High Accuracy Benchmark Problems for Allen-Cahn and Cahn-Hilliard Dynamics

Jon Matteo Church [*] Zhenlin Guo [†] Peter K. Jimack [‡]
Anotida Madzvamuse [§] Keith Promislow [¶]
Brian Wetton [‖] Stephen M. Wise [**] Fengwei Yang [††]

May 2, 2019

Abstract

There is a large literature of numerical methods for phase field models from materials science. The prototype models are the Allen-Cahn and Cahn-Hilliard equations. We present four benchmark problems for these equations, with numerical results validated using several computational methods with different spatial and temporal discretizations. Our goal is to provide the scientific community with a reliable reference point for assessing the accuracy and reliability of future software for this important class of problem.

[*]j.m.church@leeds.ac.uk, School of Computing, University of Leeds, Leeds, LS2 9JT United Kingdom

[†]zhenling@math.uci.edu, Mathematics Department, UC Irvine, Irvine, 92697-3875 USA

[‡]p.k.jimack@leeds.ac.uk, School of Computing, University of Leeds, Leeds, LS2 9JT United Kingdom

[§]A.Madzvamuse@sussex.ac.uk, University of Sussex, Brighton, BN1 9RH United Kingdom

[¶]kpromisl@math.msu.edu, Department of Mathematics, Michigan State, East Lansing, 48864 USA

[‖]wetton@math.ubc.ca, Department of Mathematics, University of British Columbia, Vancouver, V6T 1Z2 Canada

[**]swise1@utk.edu, Department of Mathematics, University of Tennessee, Knoxville, 37996-1320 USA

[††]fengwei.yang@surrey.ac.uk, Department of Chemical and Process Engineering, University of Surrey Stag Hill campus, Guildford, Surrey, GU2 7XS, United Kingdom

1 Introduction

Many material science problems require an understanding of the microstructure that develops in a mixture of two of more materials or phases over time. One model of such phenomenon is the Cahn-Hilliard (CH) [10] equation that describes phase separation of a binary alloy during annealing. The problem is described by a scalar function u of space $\mathbf{x}$ and time t that takes values $u = +1$ in one phase and $u = -1$ in the other.

$$u_t = -\epsilon^2 \Delta\Delta u + \Delta(W'(u)) \tag{1}$$

where $W(u) = \frac{1}{4}(u^2 - 1)^2$ and Δ is the Laplacian operator. The parameter ϵ in the model is a length scale – the width of the layers between the regions of different phases. Such regions form quickly and subsequently they evolve on longer time scales, generically $O(e^{C/\epsilon})$ for 1D Cahn-Hilliard [33]. In higher space dimensions formal analysis has shown that the Cahn-Hilliard model forms phase separated regions that evolve according to a Stefan problem on $O(1)$ time scale and according to a Mullins-Sekerka flow on the longer $O(\epsilon^{-1})$ time scales [32]. This analysis has been made rigorous for the Cahn-Hilliard equation with Neumann boundary conditions, [1], for periodic patterns, [2], and for patterns attached to the boundary, [3]. The study of equilibrium of the Cahn-Hilliard equation, equivalently the minimizers of the Cahn-Hilliard free energy

$$\mathcal{E}(u) := \int_\Omega \frac{1}{2}\epsilon|\nabla u^2| + \epsilon^{-1} W(u)\, dx, \tag{2}$$

has an even longer history. The key result, [31], established the $\epsilon \to 0$ limit of the Cahn-Hilliard free energy as the surface area of the interface. This result was generalized by many authors, in particular [36], see the excellent review article [34].

The Cahn-Hilliard model is in a larger family of phase field models. A review of the extensive use of such models in material science applications can be found in [11]. There are several interesting generalizations of the Cahn-Hilliard equation. Fourth order phase field models of increasing complexity are used to describe some aspects of cancerous tumour growth [45]. Sixth order models also arise in the study of network formation in functionalized polymers [20]. Because of the ubiquity and physical importance of these models, many numerical approaches have been developed to solve them, with a small sample given in the following references: [13, 39, 18, 17, 35, 16, 44].

Until now, there has been no way to evaluate the raw accuracy or the relative performance (accuracy for similar computational costs) of this array of numerical approaches. There is a set of benchmark problems described in [28]. However, these problems lack concrete numerical targets to assess accuracy. Another set of benchmark problems in [27] with radial symmetry is posed in an infinite domain, not suitable for comparison with many approaches in the literature. In this work, we propose four benchmark problems, three for Cahn-Hilliard and one for the second order Allen-Cahn equation. The problems are posed in periodic domains to allow the largest set of applicable techniques. We do not include any three dimensional (3D) problems since there is no extra structure to the dynamics in higher dimensions. The simplest form of the energy well (the canonical quartic) is considered, again to allow the largest set of computational approaches. Several methods with different spatial and temporal discretizations are applied to the benchmark problems to give confidence to the reported numerical results that can be used to assess the accuracy of other schemes. While the focus of this work is to provide numerically accurate benchmark results, we record the number of time steps and the number of iterations (conjugate gradient or multi-grid) for the different approaches and compare them in a brief discussion. We provide all the codes [48] that were used to generate the results in this paper, for the purposes of validation and reproducibility as well as to facilitate the development of improved methods or methods for related application problems. This also provides maximum clarity over all the parameters (numerical and mathematical) that have been used. Since the idea of quantitative computational benchmarks is relatively new to this research community, we provide a brief overview of their utility in Section 1.1, drawing on some examples from Computational Fluid Dynamics, where they have had an important role for several decades.

Note that our benchmark problems focus on pure materials science applications rather than the use of Cahn-Hilliard equations to track interfaces in so-called *diffuse interface methods* [50, 8] in which the CH dynamics are coupled to other physics.

In Section 2 we describe the four benchmark problems. In Sections 3 and 4 we describe the methods and results of their application to the benchmark problems, with a summary of the numerical results and our level of confidence in Section 5. We end with a short discussion.

1.1 The Utility of These Computational Benchmarks

Phase field computations have been used to model and predict morphological and microstructure evolution in materials [11]. Such computations have targets ranging from time scales for coarsening behaviour [39] to studies of metallic alloy solidification in which the objective is to obtain quantitative predictions of microstructures that are formed during the solidification process [7]. In the former case only coarse accuracy is needed while in the latter accurate quantitative predictions are required. It is typical that computational benchmark results are provided to high accuracy and that is the case in this study. A researcher using a phase field computational approach to answer an application question can get insight into the range of computational parameters needed for the required accuracy (high or low) using preliminary computations of the benchmark problems described in this work.

Computational benchmark problems have a long history in Computational Fluid Dynamics (CFD). A benchmark for the viscous, incompressible flow driven cavity problem [22] first appeared in 1982. Although it was an artificial problem, not based on any particular application, it had an important impact on the field, focussing attention on the development of accurate and efficient methods for the basic equations. More specialized benchmarks followed, with examples from multi-phase flow [26], aeronautical flows [19], and aero-acoustics [29]. In these later works, the benchmarks were for multi-physics models.

The current work for phase field model benchmarks is in the spirit of the early benchmarks in CFD, considering only basic forms of the models in simple geometries. The authors plan to use these benchmark problems to evaluate time stepping strategies and spatial discretization (adaptive versus fixed grid and time step, high order versus low order) with the goal to provide adequate accuracy for optimal computational cost. We invite other researchers to participate. Spatial discretizations considered in this work are Fourier pseudo-spectral (see also [30, 13]) and second order finite difference (see also [44, 23]). Comparison to existing fourth order finite difference [12] and mixed finite element methods [47, 49, 15] in the literature could be done. The temporal discretizations used in this work are not regularized, that is they do not guarantee energy decay (see also [13, 49]). It is an interesting question whether stabilized methods that do have this guarantee [16, 18, 35, 39, 44, 47, 30, 12, 23] will behave better or worse in practice. The well-known first order energy stable scheme [18] suffers from inaccu-

racy [13, 46] but the relative behaviour of higher order schemes is not clear. Much of the insight gained from such studies on these simple models should translate to models with more complicated physics, since most phase field models for materials science share the traits of localized spatial behaviour and meta-stable dynamics.

2 Benchmark Problems

We propose four benchmarks problems, I-IV, described below. Problems I-III have specific numerical results reported here. The benchmark for Problem IV is available online [48].

2.1 I: 2D Allen Cahn

The first benchmark is for the Allen-Cahn equation [4]:

$$u_t = \epsilon^2 \Delta u - W'(u) \tag{3}$$

where $W(u) = \frac{1}{4}(u^2 - 1)^2$ and Δ is the Laplacian operator. It describes the evolution of crystal grains of the same material during annealing. It can also be called a Ginzberg-Landau equation. It is simpler numerically than CH dynamics since it has lower order as a partial differential equation. We choose a simple 2D problem in a doubly periodic domain $[0, 2\pi]^2$ with initial conditions

$$u(x, y, 0) = \tanh \frac{\sqrt{(x-\pi)^2 + (y-\pi)^2} - 2}{\epsilon\sqrt{2}}$$

and compute with $\epsilon = 0.2$, 0.1, and 0.05. The benchmark is the time T at which the value at the domain centre (π, π) changes from negative to positive. Except for the exponentially small (in ϵ) derivative discontinuities at the periodic boundaries, the dynamics approximate the sharp interface limit of curvature motion of a circle in a time scale of ϵ^{-2}. The expectation from asymptotic analysis of the sharp interface limit is that

$$T = 2/\epsilon^2 + O(1).$$

This is confirmed by the numerical solutions below. Some snapshots of the dynamics are shown in Figure 1. A video of the dynamics is also available [41].

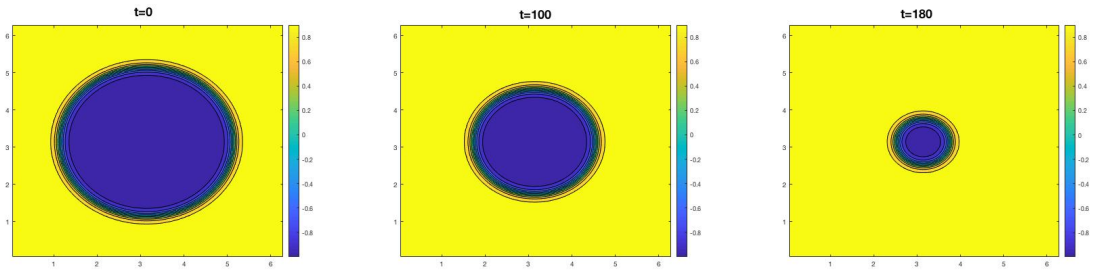

Figure 1: Benchmark I: Allen Cahn dynamics with $\epsilon = 0.1$.

i	x_i	y_i	r_i
1	$\pi/2$	$\pi/2$	$\pi/5$
2	$\pi/4$	$3\pi/4$	$2\pi/15$
3	$\pi/2$	$5\pi/4$	$2\pi/15$
4	π	$\pi/4$	$\pi/10$
5	$3\pi/2$	$\pi/4$	$\pi/10$
6	π	π	$\pi/4$
7	$3\pi/2$	$3\pi/2$	$\pi/4$

Table 1: Centres (x_i, y_i) and radii r_i of the initial conditions for benchmark II

2.2 II: 2D Cahn Hilliard seven circles

The second benchmark is for the 2D Cahn Hilliard dynamics (1), again in the doubly periodic domain $[0, 2\pi]^2$. Initial conditions are seven circles with centres and radii given in Table 1 dressed with a smooth profile:

$$u(x, y, 0) = -1 + \sum_{i=1}^{7} f(\sqrt{(x - x_i)^2 + (y - y_i)^2} - r_i)$$

with

$$f(s) = \begin{cases} 2e^{-\epsilon^2/s^2} & \text{if } s < 0 \\ 0 & \text{otherwise.} \end{cases}$$

Computations are done with $\epsilon = 0.1$, 0.05, and 0.025. Only at the smallest value of ϵ can the dynamics be considered to be of the asymptotic character of the Mullins Sekerka limit. The benchmarks are the times T_1 and T_2 at which the value at the points $(\pi/2, \pi/2)$ and $(3\pi/2, 3\pi/2)$ change from positive to

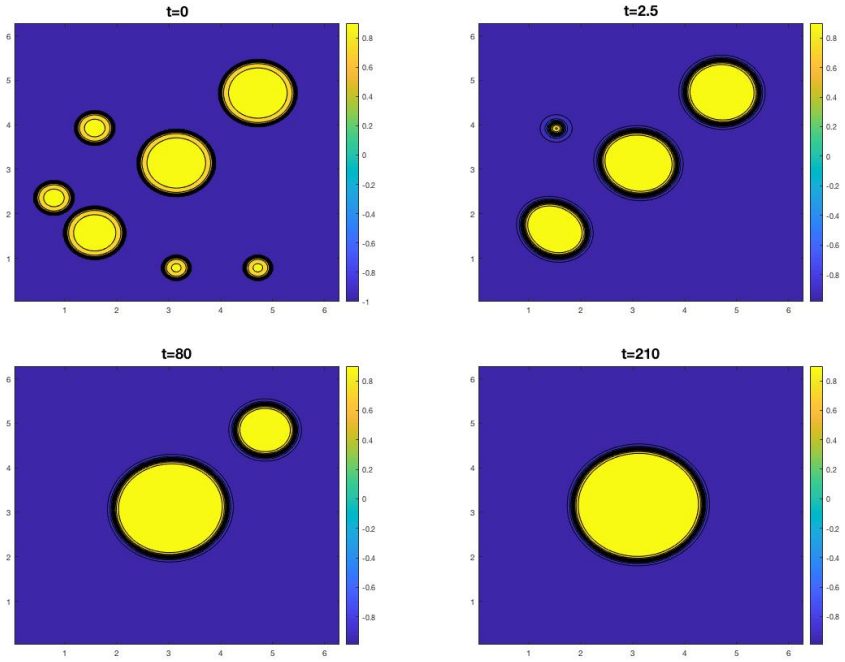

Figure 2: Benchmark II: Allen Cahn dynamics with $\epsilon = 0.05$.

negative. Some snapshots of the dynamics are shown in Figure 2. A video of the dynamics is also available [43].

2.3 III: 1D Cahn Hilliard

This problem was originally proposed in [13]. It is set in the periodic domain $x \in [0, 2\pi]$ with $\epsilon = 0.18$ and initial data

$$u(x, 0) = \cos(2x) + \frac{1}{100} e^{\cos(x+1/10)}. \tag{4}$$

Over a short time, the solution tends to two intervals each of values close to ± 1 with interfaces of width ϵ between them. The second term on the right is a small perturbation so that these intervals are not symmetric. At very large times, the intervals will slowly (exponentially slow in ϵ) evolve and merge [32, 33] as shown in Figure 3. A video of the dynamics is also available [40]. The final state with two transition layers is steady. The benchmark is the time T at which the midpoint value $u(\pi, t)$ changes from positive to

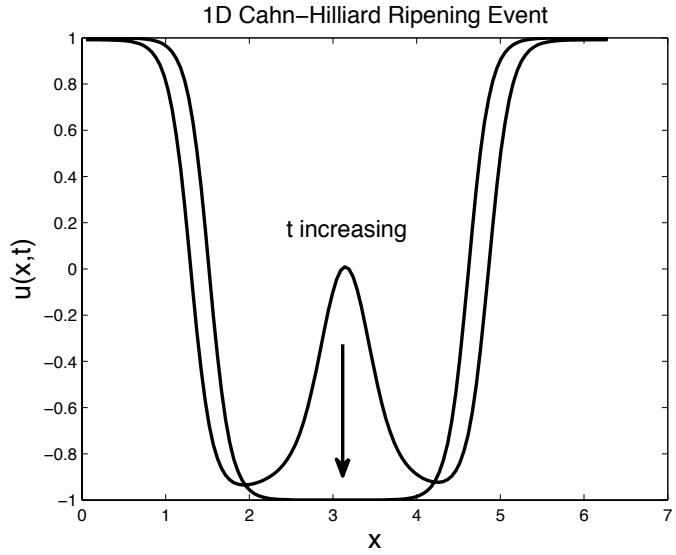

Figure 3: This figure corresponds to the solution of the 1D Cahn-Hilliard equation (1) with initial conditions (4) for $\epsilon = 0.18$ near the benchmark time.

negative. This ripening event happens at a very fast time scale after the long, slow transient. It is the wide range in time scales of the dynamics that makes this a challenging computation.

2.4 IV: 2D Cahn Hillard Energy Decay

This is a modified version of the benchmark proposed in [28]. When scaled, their formulation of Cahn Hilliard is equivalent to (1) in the $[0, 2\pi]^2$ domain with

$$\epsilon = \frac{\pi}{100}\sqrt{2/5} \approx 0.0199.$$

Their proposed initial conditions have discontinuities at the periodic boundary conditions which implies infinite initial energy, and the early dynamics are dominated by the smoothing of these discontinuities. We replace their initial conditions with smooth, periodic ones that give roughly the same energy decay that will be the target of the benchmark:

$$u(x, y, 0) = 0.05\left(\cos(3x)\cos(4y) + (\cos(4x)\cos(3y))^2 + \cos(x - 5y)\cos(2x - y)\right).$$

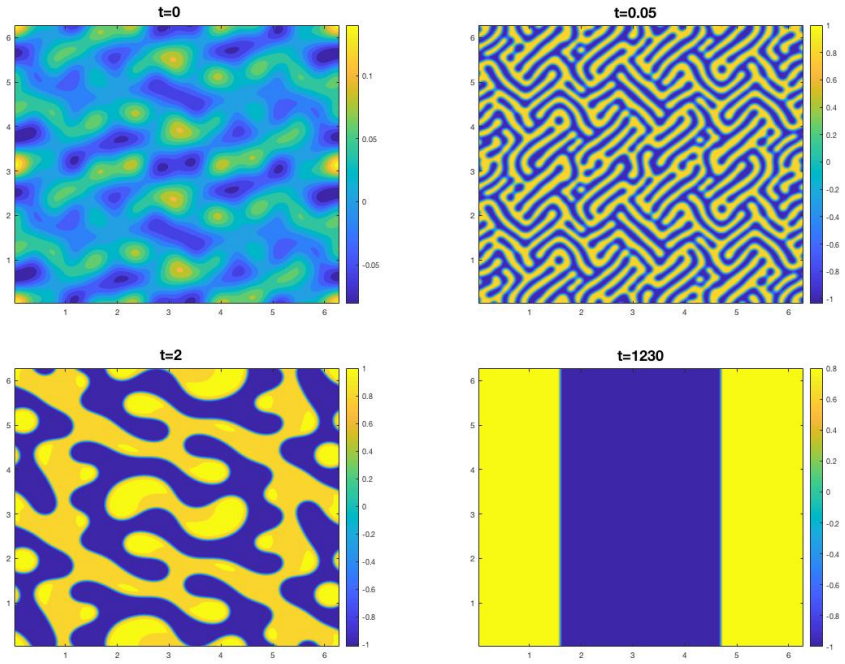

Figure 4: Benchmark IV: Cahn Hillard Energy Decay.

Some snapshots of the dynamics are shown in Figure 4 and a video of the dynamics is available [42]. The plot of $\ln \mathcal{E}$ versus $\ln t$, where $\mathcal{E}$ is the energy (2) and natural logarithms are used, is shown in Figure 5. It is the L_1 error to this function that is the benchmark. Specifically, the differences $\mathcal{D}_1$ and $\mathcal{D}_2$ between the exact $\mathcal{E}_*(t)$ and computed $\mathcal{E}_c(t)$ is given by the benchmarks

$$\mathcal{D}_1 = \int_{-5}^{7} |\ln \mathcal{E}_*(\theta) - \ln \mathcal{E}_c(\theta)| d\theta \tag{5}$$

$$\mathcal{D}_2 = \int_{-5}^{2} |\ln \mathcal{E}_*(\theta) - \ln \mathcal{E}_c(\theta)| d\theta \tag{6}$$

where $\theta = \ln t$. Pointwise values of an accurate approximation of $\mathcal{E}_*(t)$ can be found online [48]. For the accuracy reported in our computations, approximating the integrals in $\mathcal{D}_{1,2}$ with Trapezoidal rule and 1,000 equally spaced points in the interval, using linear interpolation of the computed $\mathcal{E}$ values, is sufficient.

These are proposed because often in applications the exact details of the

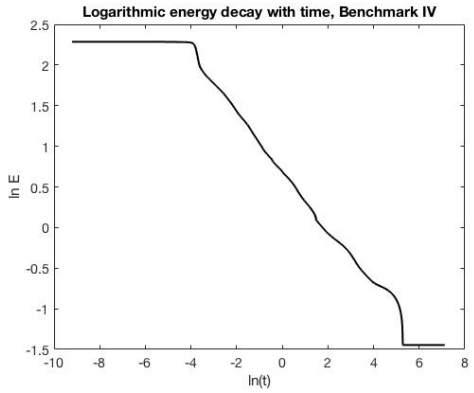

Figure 5: This figure shows the energy decay profile for the benchmark IV: 2D Cahn Hilliard problem.

computational results are not important, but the trend of the evolution of length scales is a key feature [5]. The difference $\mathcal{D}_1$ measures the difference over the full dynamics, while $\mathcal{D}_2$ covers only the first part of the dynamics and omits the fine details of the final transition to steady state. See Figure 9 to see how these details dominate the errors from under-resolved computations.

3 Methods

3.1 A: Spectral Implicit, Preconditioned Conjugate Gradient Solver, Variable Time Steps

A numerical framework that could handle a wide variety of energy gradient flows was developed in [13]. Spatial discretization is pseudo spectral [9] on a regular $N \times N$ grid with grid spacing $h = 2\pi/N$. Implicit time stepping is used, of first, second and third order accuracy. The details of the time stepping are given for a generic scalar autonomous equation $\dot{u} = f(u)$ below:

$$\text{BE:} \quad U^{n+1} = U^n + kf(U^{n+1}), \tag{7}$$

$$\text{DIRK2:} \quad U^* = U^n + \alpha k f(U^*) \tag{8a}$$

$$U^{n+1} = U^n + k(1-\alpha)f(U^*) + \alpha k f(U^{n+1}), \tag{8b}$$

$$\text{DIRK3:}\quad U^* = U^n + \gamma k f(U^*) \tag{9a}$$
$$U^+ = U^n + k(1-\gamma) f(U^*)/2 + \gamma k f(U^+) \tag{9b}$$
$$U^{n+1} = U^n + k\left(\beta_1 f(U^*) + \beta_2 f(U^+)\right) + \gamma k f(U^{n+1}) \tag{9c}$$

where k is the time step, U^n approximates $u(nk)$, Backward Euler (BE) is first order accurate, and DIRK2 and DIRK3 are second and third order Diagonally Implicit Runge Kutta methods, respectively. The DIRK variants chosen here have good stability properties for stiff problems [24] (they are L- and A-stable). The parameters are $\alpha = 1 - 1/\sqrt{2}$, γ is the middle root of $6\gamma^3 - 18\gamma^2 + 9\gamma - 1 = 0$, $\beta_1 = -3\gamma^2/2 + 4\gamma - 1/4$, and $\beta_2 = 3\gamma^2/2 - 5\gamma + 5/4$.

The implicit time stepping problems are solved using Newton iterations, with a Preconditioned Conjugate Gradient (PCG) solver for the linear system at each iteration as described in [13]. The implicit problems are convex and have have unique solutions when $k < 1$ (AC) and $k < \epsilon^2$ (CH) for BE as shown in [46]. Note that in that reference the equations are scaled differently than in the current work.

Adaptive time stepping is used. Time accuracy is controlled by specifying a local error tolerance σ. The local error for BE is estimated using a Forward Euler predictor as done in [13]. Time steps are then adjusted to maintain a local error smaller than σ for each time step. For the DIRK schemes, a predictor with higher order local accuracy V at time level $n+1$ is used. It is constructed using the computed solutions at time levels n and $n+1$ as follows:

$$V = U^n + \frac{k}{6}\left(f(U^n) + 4f(U^{n+1/2}) + f(U^{n+1})\right)$$

where $U^{n+1/2}$ is the cubic Hermite interpolant

$$U^{n+1/2} = \frac{1}{2}\left(U^n + U^{n+1}\right) + \frac{k}{8}\left(f(U^n) - f(U^{n+1})\right).$$

Benchmark transition time estimates are determined by linear interpolation between the two computed values on either side of the transition event.

3.2 B: Finite Difference Explicit, Fixed Time Steps

This approach represents the simplest possible schemes to implement, based upon second order five point finite difference stencils for spatial discretization

and explicit time stepping. The spatial discretization has been implemented using the Uintah Computational Framework, which brings support for both cell- and vertex-based discretizations as well as mesh adaptivity and parallel execution [14]. For the computation of the proposed benchmarks, however, mesh adaptivity has not been adopted and regular grids with spacing $h = 2\pi/N$ have been used. The approximation of the biharmonic operator has been performed by introducing an auxiliary variable $v = \Delta u$ and splitting equation (1) which leads to the following system:

$$\begin{cases} u_t = -\epsilon^2 \Delta v + \Delta(W'(u)) \\ v = \Delta u. \end{cases}$$

An explicit Forward Euler (FE) time discretization has been adopted with fixed time step which, using the same notation used for the previous implicit schemes, is detailed as follows:

$$\text{FE:} \qquad U^{n+1} = U^n + kf(U^n). \tag{10}$$

This method is first order accurate and conditionally stable; as a consequence, for some of the benchmark problems reported in the following, the level of spatial accuracy required resulted in a maximum stable time step that is too small to be able to perform runs of sufficient simulation time with this method.

As for the previous implementation, benchmark transition time estimates are determined by linear interpolation between the two computed values on either side of the transition event.

3.3 C: Finite Difference Implicit Multi-Grid, Fixed Time Steps

We describe our Multigrid (MG) solvers for BDF2 finite difference schemes for the Cahn-Hilliard equation. The results of two different implementations of the same approach, which we label as Ca [44] and Cb [49], are shown in this work. The differences in implementation are outlined in Section 3.3.1 below.

Spatially, the finite difference method decompose the continuous domain into number of uniform grids, and the standard 5-points stencil is employed

that guarantees the 2nd order accuracy. Temporally, the second order accurate BDF2 is employed. In particular the method can be illustrated as

$$u^{n+1} - \frac{2}{3}k\Delta(\mu^{n+1}) = \frac{4}{3}u^n - \frac{1}{3}u^{n-1}, \tag{11}$$

$$-W'(u^{n+1}) + \epsilon^2\Delta u^{n+1} + \mu^{n+1} = 0, \tag{12}$$

where we split the 4th order CH model into two 2nd order PDEs by introducing a chemical potential $\mu = -\epsilon^2\Delta u + W'(u)$. Here we set $u^0 = u^{-1} = u_{initial}$ at the very first time step. Moreover, we employ a fixed time step k for the simulations. The second-order scheme is then equivalent to the following: find $u, \mu \in \mathcal{C}_{\text{per}}$ (simultaneously) whose components satisfy

$$u_{i,j} - \frac{2}{3}k\ \Delta_h\mu_{i,j} = \frac{4}{3}u^n_{i,j} - \frac{1}{3}u^{n-1}_{i,j}, \tag{13}$$

$$\mu_{i,j} - u^3_{i,j} + u_{i,j} + \epsilon^2\Delta_h u_{i,j} = 0, \tag{14}$$

where we have dropped the time superscripts $n+1$ on the unknowns. Here $\mathcal{C}_{\text{per}}$ denotes the sets of cell-centred grid variables with periodic boundary conditions, and Δ_h denotes the discrete difference operator (h is the uniform grid spacing). See [44, 49] for more details. The AC equations are similar, and so we omit the implementation details for brevity. We use a nonlinear FAS multigrid method to solve the system (13) – (14) efficiently. This involves defining operator and source terms, which we do as follows. Let $\mathbf{U} = (u, \mu)^T$. Define the nonlinear operator $\mathbf{N} = (N^{(1)}, N^{(2)})^T$ as

$$N^{(1)}_{i,j}(\mathbf{U}) = u_{i,j} - \frac{2}{3}k\ \Delta_h\mu_{i,j}, \tag{15}$$

$$N^{(2)}_{i,j}(\mathbf{U}) = \mu_{i,j} - u^3_{i,j} + u_{i,j} + \epsilon^2\Delta_h u_{i,j}, \tag{16}$$

and the source $\mathbf{S} = (S^{(1)}, S^{(2)})^T$ as

$$S^{(1)}_{i,j}(\mathbf{U}) = \frac{4}{3}u^n_{i,j} - \frac{1}{3}u^{n-1}_{i,j}, \tag{17}$$

$$S^{(2)}_{i,j}(\mathbf{U}) = 0. \tag{18}$$

We will describe a somewhat standard nonlinear FAS multigrid scheme for solving the vector equation $\mathbf{N}(\mathbf{U}^{n+1}) = \mathbf{S}(\mathbf{U}^n, \mathbf{U}^{n-1})$. The action of this operator is represented as

$$\widetilde{\mathbf{U}} = \text{Smooth}(\lambda, \mathbf{U}, \mathbf{N}, \mathbf{S}), \tag{19}$$

where $\mathbf{U}$ is an approximate solution prior to smoothing, $\widetilde{\mathbf{U}}$ is the smoothed approximation, and λ is the number of smoothing sweeps. For smoothing we use a nonlinear Gauss-Seidel method with Red-Black ordering. In what follows, to simplify the discussion, we give the details of the relaxation using the simpler lexicographic ordering. Let ℓ be the index for the lexicographic Gauss-Seidel. (Note that the smoothing index ℓ in the following should not be confused with the time step index n.)

The Gauss-Seidel smoothing is as follows: for every (i, j), stepping lexicographically from $(1, 1)$ to (N, N), find $u_{i,j}^{\ell+1}$ and $\mu_{i,j}^{\ell+1}$ that solve

$$u_{i,j}^{\ell+1} + \frac{8\tau}{3h^2}\mu_{i,j}^{\ell+1} = S_{i,j}^{(1)}\left(\mathbf{U}^n, \mathbf{U}^{n-1}\right) + \frac{2\tau}{3h^2}\Big(\mu_{i+1,j}^{\ell} + \mu_{i-1,j}^{\ell+1} + \mu_{i,j+1}^{\ell} + \mu_{i,j-1}^{\ell+1}\Big), \quad (20)$$

$$\left(-(u_{i,j}^{\ell})^2 + 1 - \frac{4\epsilon^2}{h^2}\right) u_{i,j}^{\ell+1} + \mu_{i,j}^{\ell+1} = S_{i,j}^{(2)}\left(\mathbf{U}^n\right) - \frac{\epsilon^2}{h^2}\Big(u_{i+1,j}^{\ell} + u_{i-1,j}^{\ell+1} + u_{i,j+1}^{\ell} + u_{i,j-1}^{\ell+1}\Big). \quad (21)$$

Note that we have linearized the cubic term using a local Picard-type approximation and lagged the non-convex term (to avoid solvability conditions), but otherwise this is a standard vector application of block Gauss-Seidel. We then use Cramer's Rule to obtain $u_{i,j}^{\ell+1}$ and $\mu_{i,j}^{\ell+1}$.

This is then followed by a standard V-cycle structure, which involves the restriction operator that transfers fine grid functions to the coarse grid, and prolongation operator that transfers coarse grid functions to the fine grid. The operators communicate information from coarse levels to fine levels, and *vice versa*. Moreover, the tolerance is L_2 norm residual of all the variables, and is required to be less than 10^{-10} for all the computations. Here we refer to Trottenberg *et al.* [38, Sec. 5.3] and our paper [44] for complete details of scheme Ca and to [6, 49] for details of scheme Cb.

3.3.1 Differences in the implementations Ca and Cb

Coarsest grid correction:

Ca: Fixed at 2 iterations for all examples.

Cb: Fixed iterations with a choice of 15 for benchmark I, 40 for the other 2D examples and 100 for the 1D CH problem.

Iterative Solver:

Ca: Full Gauss Seidel (GS).

Cb: Jacobi on partition edges and GS otherwise.

Stopping tolerance of solver at each time step (both use value 10^{-10}):

Ca: Average mean squared residual (L2) over variables u and μ.

Cb: Maximum mean squared residual (L2) over variables u and μ.

4 Benchmark Results

4.1 I: 2D Allen Cahn

We present full details of our numerical tests for this problem, so the reader can see how we judge our accuracy conclusions to the benchmarks.

4.1.1 I-A: 2D Allen Cahn, Spectral Implicit PCG

Details of the convergence study for $\epsilon = 0.2$ are shown in Table 2. The results are computed with spatial resolution $N = 128$ for $\epsilon = 0.2$ and 0.01, and $N = 256$ for $\epsilon = 0.05$ and the results do not change in the digits shown when the spatial resolution is doubled. In terms of the benchmark value, there is clear asymptotic convergence in σ for all three schemes and a clear conclusion

$$T = 48.17 \pm 0.01 \quad \text{for } \epsilon = 0.2$$

can be drawn from the computations. The methods have local truncation error $O(k^{p+1})$ with $p = 1, 2, 3$ for BE, DIRK2, and DIRK3 respectively. Thus, we expect to have a number of time steps M that behaves like

$$M = O(\sqrt[p+1]{\sigma})$$

and since $\sqrt{10} \approx 3.16$, $\sqrt[3]{10} \approx 2.15$, and $\sqrt[4]{10} \approx 1.78$ this behaviour is clearly seen in the data, validating the adaptive time stepping strategy. There is a

	BE			DIRK2			DIRK3		
σ	M (ratio)	CG	T	M (ratio)	CG	T	M (ratio)	CG	T
10^{-4}	694	3,103	48.103	171	1,995	48.287	136	2,883	48.365
10^{-5}	2,132 (3.07)	7,515	48.143	331 (1.94)	2,929	48.217	230 (1.69)	3,363	48.269
10^{-6}	6,701 (3.14)	18,723	48.155	680 (2.05)	4,951	48.1864	408 (1.71)	5,540	48.220
10^{-7}	21,164 (3.16)	42,322	48.159	1,441 (2.12)	8,232	48.173	734 (1.80)	8,240	48.194
10^{-8}	70,098 (3.31)	136,009	48.161	3,089 (2.14)	17,243	48.167	1,330 (1.81)	11,510	48.179

Table 2: I-A results for $\epsilon = 0.2$, with σ the local error tolerance, M the number of time steps (with the ratio to the value above), CG the number of conjugate gradient iterations, and T the computed approximation of the transition time.

large increase in computational efficiency moving from BE to DIRK2, and a much less significant increase from DIRK2 to DIRK3. This is also seen in the smaller ϵ computations. It is also seen that the number of CG iterations per time step goes down as σ (and so the time step k) decreases. This is consistent with the estimates on the condition number of the preconditioner in [46].

The same careful computational study leads to

$$\begin{aligned} T &= 197.72 \pm 0.01 \quad \text{for } \epsilon = 0.1 \\ T &= 797.26 \pm 0.01 \quad \text{for } \epsilon = 0.05. \end{aligned}$$

For completeness, graphs of the time step size $k(t)$ and the energy $E(t)$ for the $\epsilon = 0.1$, $\sigma = 10^{-4}$ calculation are shown in Figure 6.

4.1.2 I-B: 2D Allen Cahn, Finite Difference Explicit

The number N of mesh cells used to spatially discretize the computational domain has been chosen to make the domain center coincide with a computational point: either a cell center or a grid node, depending on the chosen representation (i.e. cell-centered or vertex-based finite differences). For each choice of N, increasingly small time steps have been considered and the corresponding benchmark time computed. From these values it has also been possible to estimate the order of convergence in space and time of this method. Results for $\epsilon = 0.2$ are reported in Table 3.

It is possible to extrapolate the results in Table 3 in mesh size based upon the last two grids. For example, the vertex-based scheme has a difference of $48.1973 - 48.1702 = 0.0271$. If this is quartered for each subsequent

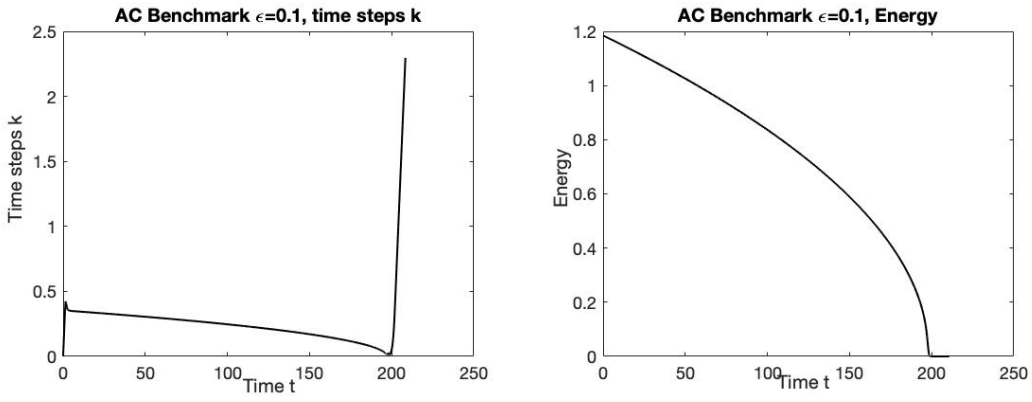

Figure 6: Time steps k (chosen adaptively with BE) and Energy E for the I-A benchmark computation for $\epsilon = 0.1$ and local error tolerance $\sigma = 10^{-4}$.

	cell centered				vertex based			
k	N	T	$O(k)$	$O(1/N)$	N	T	$O(k)$	$O(1/N)$
$3\ 10^{-2}$	63	48.8126			64	48.7928		
$9\ 10^{-3}$	63	48.7867			64	48.7670		
$3\ 10^{-3}$	63	48.7793	1.17		64	48.7596	1.16	
$9\ 10^{-4}$	63	48.7767	0.85		64	48.7570	0.86	
$3\ 10^{-4}$	63	48.7760	1.17		64	48.7563	1.17	
$9\ 10^{-5}$	63	48.7757	0.86		64	48.7560	0.86	
$9\ 10^{-3}$	127	48.3194			128	48.3171		
$3\ 10^{-3}$	127	48.3122			128	48.3098		
$9\ 10^{-4}$	127	48.3096	0.86		128	48.3073	0.86	
$3\ 10^{-4}$	127	48.3089	1.16		128	48.3066	1.16	
$9\ 10^{-5}$	127	48.3086	0.86		128	48.3063	0.86	
$3\ 10^{-3}$	255	48.2011		2.09	256	48.2008		2.06
$9\ 10^{-4}$	255	48.1985		2.09	256	48.1982		2.06
$3\ 10^{-4}$	255	48.1978	1.17	2.09	256	48.1975	1.17	2.06
$9\ 10^{-5}$	255	48.1976	0.85	2.09	256	48.1973	0.86	2.06
$9\ 10^{-4}$	511	48.1712		2.03	512	48.1712		2.01
$3\ 10^{-4}$	511	48.1705		2.03	512	48.1705		2.01
$9\ 10^{-5}$	511	48.1702	0.86	2.03	512	48.1702	0.86	2.01

Table 3: I-B results for $\epsilon = 0.2$, with k the time step size N the number of grid cells, $O(k)$ the estimated order of convergence in time, $O(1/N)$ the estimated order of convergence in space, and T, the computed approximation of the transition time.

grid level it gives the sequence $0.0068, 0.0017, 0.0004, 0.0001$ which yields the extrapolated value of 48.1612. A similar conclusion holds for the cell-centered case.

The equivalent convergence study for smaller choices of ϵ gives the following results:

$$\begin{aligned} T &\rightarrow 197.71 \quad \text{for } \epsilon = 0.1, \\ T &\rightarrow 797.17 \quad \text{for } \epsilon = 0.05. \end{aligned}$$

4.1.3 I-C: 2D Allen Cahn, Finite Difference Implicit MG

Implementation Ca

We compute the proposed Allen-Cahn system with different values of ϵ (=0.2, 0.1, 0.05). For each ϵ, we start from a relatively coarse uniform grid, for example 128×128, and a large time step, $k = 10^{-2}$. For each grid, we take $1/10$ of the time step k up to 10^{-4}, until we can obtain a convergent result of T_1. Then we move to the next refined gird to obtain the corresponding convergent T_1. Here we show our results in Table 4.

Grid	$\epsilon = 0.2$	$\epsilon = 0.1$	$\epsilon = 0.05$
128×128	48.3100	200.1336	843.2275
256×256	48.2005	198.3112	806.6749
512×512	48.1710	197.8559	799.6715

Table 4: Convergence results for AC model with different ϵ.

From the results presented in Table 4, we observe the overall 2nd order convergence rate. Therefore we deduce the asymptotic convergence of the specified stopping criteria T_1 is towards

$$\begin{aligned} T_1 = 48.161 \quad &\text{for} \quad \epsilon = 0.2, \\ T_1 = 197.710 \quad &\text{for} \quad \epsilon = 0.1, \\ T_1 = 797.171 \quad &\text{for} \quad \epsilon = 0.05. \end{aligned}$$

Implementation Cb

We solve the proposed Allen-Cahn model with three different ϵ, namely 0.2, 0.1 and 0.05 respectively. For each value of ϵ, we start with a grid of

64×64 and a time step size $k = 0.1$ if possible. We halve k each time towards 0.003125 (if needed) to see the convergence in T. Then we refine the grid towards 512×512 and halving k on every different grid to obtain the convergence results. We illustrate these computational results in Table 5.

Grid	$\epsilon = 0.2$	$\epsilon = 0.1$	$\epsilon = 0.05$
64×64	48.725	208.838	-
128×128	48.3	200.138	843.231
256×256	48.2	198.3	807.163
512×512	48.175	197.856	799.675

Table 5: Convergence results for the Allen-Cahn model, we report the converged T for each grid after repeatedly halving the time step k.

From the computational results presented in Table 5, we can confirm the asymptotic convergence to the specified stopping criteria (i.e. T) with $\epsilon = 0.2$ is 48.17. Our computational results for $\epsilon = 0.1$ and $\epsilon = 0.05$ may be extrapolated based on the observed second-order convergence (via using second-order schemes in both spatial and temporal domains), to deduce the convergence of T when $\epsilon = 0.1$ towards 197.71 and when $\epsilon = 0.05$ towards 797.18.

4.2 II: 2D Cahn Hilliard Seven Circles

4.2.1 II-A: 2D Cahn Hilliard Seven Circles, Spectral Implicit PCG

Following the same strategy of refinement in temporal and spatial approximation with the adaptive time stepping as done in Section 4.1.1, the benchmark estimates are shown in Table 6. Because of the limited increase in accuracy going from DIRK2 to DIRK3 observed in Section 4.1.1, only BE and DIRK2 time stepping were used for this benchmark.

For completeness, graphs of the time step size $k(t)$ and the energy $E(t)$ for the $\epsilon = 0.05$, $\sigma = 10^{-4}$ calculation are shown in Figure 7. The number of time steps and CG iterations for $\sigma = 10^{-4}$ are listed in Table 7. Note that for this modest accuracy requirement, DIRK2 becomes less efficient than BE as $\epsilon \to 0$. For this reason, we only use BE for the benchmark IV-A computation in Section 4.4.1. This unexpected behaviour in higher order methods will be investigated by the authors in future work.

ϵ	T_1	T_2
0.1	6.34 $\pm$ 0.01	26.01 $\pm$ 0.01
0.05	38.13 $\pm$ 0.01	94.98 $\pm$ 0.01
0.025	107.4 $\pm$ 0.01	233.20 $\pm$ 0.01

Table 6: Estimates for benchmark II (CH seven circles) using the time adaptive spectral method.

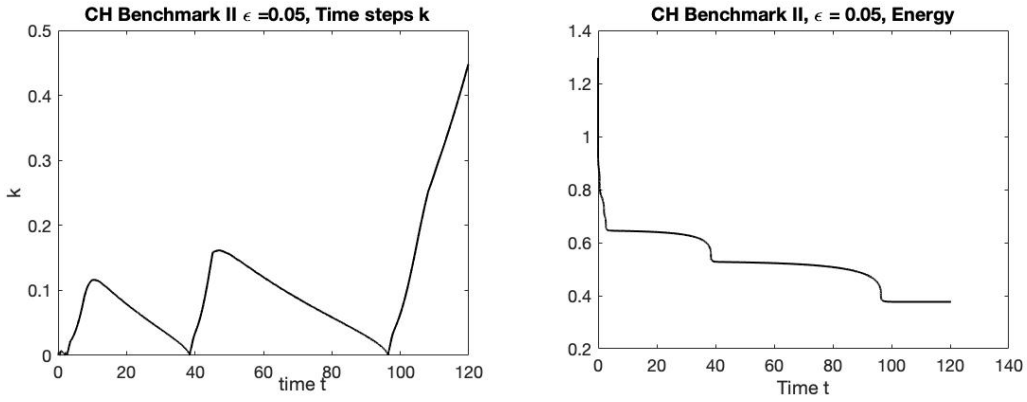

Figure 7: Time steps (chosen adaptively for BE) and energy for the II-A benchmark computation for $\epsilon = 0.05$ and local error tolerance $\sigma = 10^{-4}$.

	BE		DIRK2	
ϵ	M	CG	M	CG
0.1	2,040	45,496	850	28,227
0.05	4,835	145,959	3,722	133,828
0.025	9,354	403,445	12,985	522,096

Table 7: II-A computational details for $\sigma = 10^{-4}$, with M the number of time steps and CG the number of conjugate gradient iterations.

	cell centered			vertex based		
k	N	T_1	T_2	N	T_1	T_2
10^{-4}	62	6.6699	25.6796	64	6.6428	26.6155
10^{-5}	62	6.6697	26.6794	64	6.6427	26.6153
10^{-6}	62	6.6697	26.6794	64	6.6427	26.6153
10^{-5}	126	6.3957	26.2164	128	6.3964	26.1783
10^{-6}	126	6.3957	26.2164	128	6.3964	26.1782
10^{-6}	254	6.3509	26.0519	256	6.3508	26.0509

Table 8: II-B. Computed approximations of the transition times T_1, T_2 for $\epsilon = 0.1$.

4.2.2 II-B: 2D Cahn Hilliard Seven Circles, Finite Difference Explicit

The same criterion for choosing both spatial and temporal discretization steps has been used. For this application, however, the stability constraint associated with the explicit time step becomes a practical barrier as N increases, which means that even for $\epsilon = 0.1$ we have only just started to approach the asymptotic regime that allows us to extrapolate values for T_1 and T_2 in the limit as $N \to \infty$. Smaller values of ϵ require finer spatial discretization steps which correspond to even more restrictive choices of timestep and are therefore not reported.

Results are shown in Table 8 for $\epsilon = 0.1$. Extrapolation based on second order convergence yields improved estimates of $T_1 \approx 6.34$ and $T_2 \approx 26.01$ (for the vertex based scheme).

4.2.3 II-C: 2D Cahn Hilliard Seven Circles, Finite Difference Implicit MG

Implementation Ca

We employ the same strategy to solve this 2D Cahn Hilliard model with an initial condition that consists of seven circles. Three values of ϵ are used here, namely 0.1, 0.05 and 0.025. The spatial refinement starts from a grid of 128×128 and a time step size $k = 0.0016$, if possible. We halve k each time towards 0.0001 and refine the grid towards 512×512. We illustrate our convergence results in Table 9.

Implementation Cb

We employ the same strategy to solve this 2D Cahn Hilliard model with an initial condition that consists of seven circles. There are three choices of

Grid	$\epsilon = 0.1$		$\epsilon = 0.05$		$\epsilon = 0.025$	
	T1	T2	T1	T2	T1	T2
128×128	6.3829	26.1766	39.1786	96.4759	-	-
256×256	6.3502	26.0503	38.2832	95.3785	111.763	251.3453
512×512	6.3412	26.0194	38.1630	95.0755	107.8016	233.4128

Table 9: Convergence results for the 2D Cahn Hilliard Seven Circles model, we report the converged $T1$ and $T2$ for each grid after repeatedly halving the time step k.

ϵ, namely 0.1, 0.05 and 0.025. The spatial refinement starts from a grid of 64×64 and a time step size $k = 0.01$, if possible. We halve k each time towards 0.000625 and refine the grid towards 512×512. We illustrate our convergence results in Table 10.

	$\epsilon = 0.1$		$\epsilon = 0.05$		$\epsilon = 0.025$	
Grid	T_1	T_2	T_1	T_2	T_1	T_2
64×64	6.43	27.02	-	-	-	-
128×128	6.39	26.21	39.18	96.73	-	-
256×256	6.35	26.07	38.29	95.51	111.764	251.666
512×512	6.34	26.03	38.16	95.14	107.802	233.920

Table 10: Convergence results for the 2D Cahn Hilliard Seven Circles model, we report the converged T_1 and T_2 for each grid after repeatedly halving the time step k.

4.3 III: 1D Cahn-Hillard

4.3.1 III-A: 1D Cahn-Hillard, Spectral Implicit PCG

For this problem, adaptive time stepping allows the solver to follow the dynamics, as shown in Figure 8. DIRK2 and DIRK3 provide a considerable accuracy benefit.

Estimates for the benchmark time from this computational method are $T = 8318.6 \pm 0.1$. We include computed transition times for smaller ϵ values, although these are not verified by the other computational methods:

$\epsilon = 0.16$**:** $T = 34317.7 \pm 0.1$,

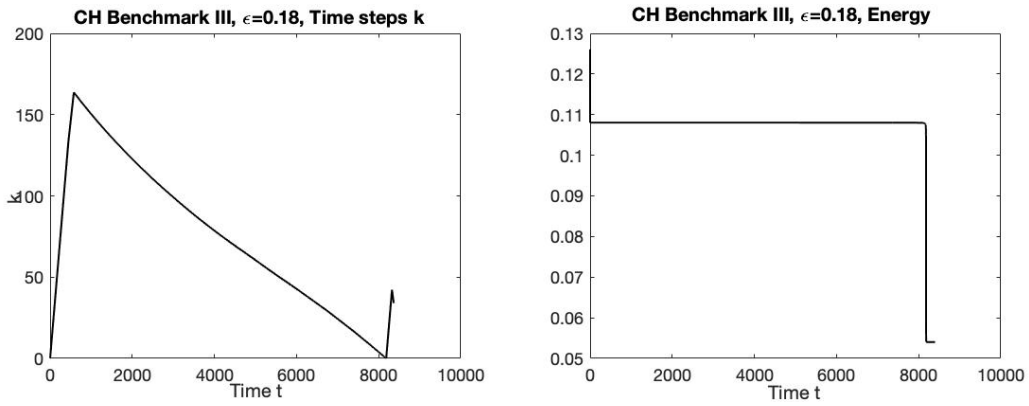

Figure 8: Time steps (chosen adaptively) and energy for the III-A benchmark computation for $\epsilon = 0.18$ using the Spectral Solver with Backward Euler time stepping, local error tolerance $\sigma = 10^{-4}$.

k	cell centered ($N = 63$)	vertex based ($N = 64$)
$3\ 10^{-4}$	7347.3036	7282.6372
$9\ 10^{-5}$	7347.2837	7282.6174
$3\ 10^{-5}$	7347.2779	7282.6117

Table 11: III-B. Computed approximations of the transition time T_1.

$\epsilon = 0.15$**:** $T = 82217.4 \pm 0.1$.

These results are obtained with DIRK3 time stepping. The exponentially slow nature of the dynamics can be seen from these results.

4.3.2 III-B: 1D Cahn Hilliard, Finite Difference Explicit

For this application the spatial resolution required to describe accurately the evolution of the field u imposes a time step stability constraint that is simply too restrictive to perform accurate simulation using this explicit scheme. Only simulation with $N = 63$ and $N = 64$ could be performed with the cell-centered and vertex-based schemes respectively and their results are reported in Table 11.

4.3.3 III-C: 1D Cahn-Hillard, Finite Difference Implicit MG

Implementation Ca

For this problem, we start with a grid of 128 and a time step size $k = 0.01$. We refine both towards 8192 and $k = 0.0001$, respectively. We report our computational results from setting $\epsilon = 0.18$ in Table 12. Note that extrapolation based on second order convergence gives $T \approx 8320.48$.

Grid	T
128	8067.9822
256	8254.7649
512	8302.8837
1024	8315.0039
2048	8319.0439
4096	8320.1439
8192	8320.3964

Table 12: Convergence results for the 1D Cahn Hilliard, we report the converged T for each grid after repeatedly halving the time step k.

Implementation Cb

For this problem, we start with a grid of 256 and a time step size $k = 0.1$. We refine both towards 4096 and $k = 0.0015625$, respectively. We report our computational results from setting $\epsilon = 0.18$ in Table 13. Note that extrapolation based on second order convergence gives $T \approx 8320.47$.

Grid	T
256	8254.2
512	8302.3
1025	8314.42
2048	8317.46
4096	8318.22

Table 13: Convergence results for the 1D Cahn Hilliard, we report the converged T for each grid after repeatedly halving the time step k.

σ	$\mathcal{D}_1$
10^{-4}	
$5 \cdot 10^{-5}$	0.44
$2 \cdot 10^{-5}$	1.5
10^{-5}	0.61
$5 \cdot 10^{-6}$	0.023
$2.5 \cdot 10^{-6}$	0.0039

Table 14: Convergence of the logarithmic energy profile for benchmark IV in $\mathcal{D}_1$ defined in (5) with local time step error tolerance σ for the spectral solver. The values of $\mathcal{D}_1$ shown are to the computation with σ from the line above.

4.4 IV: 2D Cahn-Hillard Energy Decay

4.4.1 IV-A: 2D Cahn-Hillard Energy Decay, Spectral Implicit PCG

It was found that $N = 384$ was sufficient to give values of the logarithmic energy integrals that define $\mathcal{D}_{1,2}$ (5) and (6) with spatial errors less than 10^{-4} for a range of local error tolerance values σ. The convergence in the energy profile as the local time step tolerance σ is refined is shown in Table 14 and Figure 9. The most refined energy profile for $\sigma = 2.5 \times 10^{-5}$ is the profile submitted as the most accurate benchmark at [48]. From the convergence analysis shown in Table 14 there is evidence that the submitted profile is accurate with $\mathcal{D}_{1,2} \leq 4 \cdot 10^{-3}$.

4.4.2 IV-B: 2D Cahn Hilliard Energy Decay, Finite Difference Explicit

For this application simulations have been performed for $N = 96, 192, 384$ using cell-centered spatial discretizations. One choice of timestep k to ensure numerically stability has been used for each grid size. It was found that only $N = 384$ yielded spatial accuracy to ensure that the solution eevolves to a reasonable approximation of the correct energy profile. The convergence in the Energy profile as the grid and time step are refined is shown in Table 15.

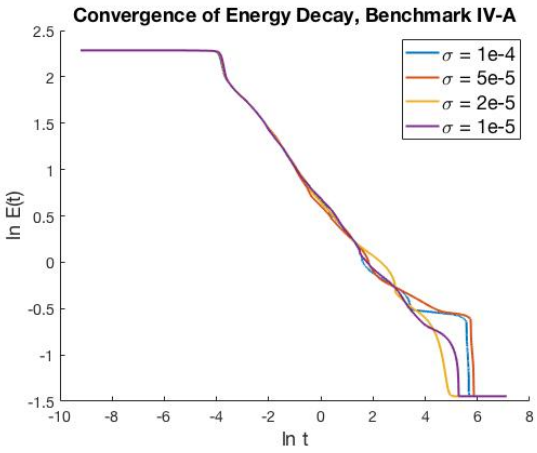

Figure 9: The numerical convergence of the energy decay profile for the benchmark IV: 2D Cahn Hilliard problem, with the spectral solver with local time step error tolerance σ. Smaller values of σ give profiles that are not visually different.

k	N	$\mathcal{D}_1$	$\mathcal{D}_2$
$4.2 \cdot 10^{-4}$	96	$1.2 \cdot 10^{1}$	$2.7 \cdot 10^{0}$
$5.4 \cdot 10^{-5}$	192	$1.1 \cdot 10^{0}$	$5.1 \cdot 10^{-1}$
$4.8 \cdot 10^{-6}$	384	$6.0 \cdot 10^{-1}$	$3.2 \cdot 10^{-1}$

Table 15: Convergence of the logarithmic Energy profile for benchmark IV-B in $\mathcal{D}_1$ (5) and $\mathcal{D}_2$ (6) for the finite difference solver.

4.4.3 IV-C: 2D Cahn-Hilliard Energy Decay, Finite Difference Implicit MG

Implementation Ca

The differences between our numerical results $\mathcal{E}_c$ obtained on different meshes (128×128, 256×256 and 512×512) and the benchmark energy profile, $\mathcal{E}_*$, are shown in Table 16.

Grid	$\mathcal{D}_1$	$\mathcal{D}_2$
128	1.0221×10^{1}	1.7910×10^{0}
256	9.1202×10^{-1}	1.4479×10^{-1}
512	8.5579×10^{-1}	1.3803×10^{-1}

Table 16: Convergence results for the energy decay of 2D Cahn Hilliard problem, we report the converged energy profile for each grid after repeatedly halving the time step k.

5 Summary of Benchmark Results

Our benchmark numerical results are summarized in Table 17, with confidence on the values based on the agreement we achieved between the four schemes.

6 Discussion

We have provided computational benchmarks for Allen-Cahn and Cahn-Hilliard dynamics in periodic geometries, carefully validated using different spatial and temporal discretizations. We believe these benchmarks, and also the implementations we used for the results that are available online [48], will be useful in the evaluation of current methods and the development of new ones. Future benchmarks in the field could include higher order equations [21, 25, 37] and more complicated energy wells such as Flory-Huggins.

The accurate benchmark values can be used to investigate the properties of other time stepping schemes. They can also play a role in the investigation of the computational advantages of adaptive time stepping and adaptive spatial grids. There is a large application community that uses these models,

Benchmark	value	all	two
I, $\epsilon = 0.2$	T	48.16 ± 0.01	48.16 ± 0.01
I, $\epsilon = 0.1$	T	197.71 ± 0.01	197.71 ± 0.01
I, $\epsilon = 0.05$	T	797.2 ± 0.1	797.17 ± 0.01
II $\epsilon = 0.1$	T_1	6.34 ± 0.01	6.34 ± 0.01
II $\epsilon = 0.1$	T_2	26.02 ± 0.01	26.02 ± 0.01
II $\epsilon = 0.05$	T_1		38.15 ± 0.02
II $\epsilon = 0.05$	T_2		95.1 ± 0.2
II $\epsilon = 0.025$	T_1		107 ± 1
II $\epsilon = 0.025$	T_2		233 ± 1
III	T	8000 ± 1000	8319 ± 2
IV	$\mathcal{D}_1$	±0.9	± 0.6
IV	$\mathcal{D}_2$	±0.32	± 0.14

Table 17: Summary of benchmark results. The "all" column lists the result on which all four schemes agree up to the indicated tolerance and "two" on which at least two schemes agree.

or variants, in their computational studies, and a large community of theoreticians interested in designing and proving convergence of new methods. Having the fixed target presented in the current work will help direct the research towards more efficient schemes.

Acknowledgements

PKJ acknowledges support from EPSRC grant EP/N007638/1. AM acknowledges partial funding from the European Union Horizon 2020 research and innovation programme under the Marie Sklodowska-Curie grant agreement No 642866. This work (FYW, AM) was partly supported by the Leverhulme Trust Research Project Grant (RPG-2014-149). AM is a Royal Society Wolfson Research Merit Award Holder funded generously by the Wolfson Foundation. KP recognizes support from the NSF DMS under award 1813203. SW recognizes support from the NSF DMS under award 1719854. BW acknowledges support from an NSERC Canada grant.

References

[1] N. Alikakos, P. Bates, and X. Chen. Convergence of the cahn-hilliard equation to the hele-shaw model. *Archive for Rational Mechanics and Analysis*, 128(2):165–205, 6 1994.

[2] N. D. Alikakos, P. W. Bates, and X. Chen. Periodic traveling waves and locating oscillating patterns in multidimensional domains. *Transactions of the American Mathematical Society*, 351(7):2777 – 2805, 1999.

[3] N. D. Alikakos, P. W. Bates, X. Chen, and G. Fusco. Mullins-sekerka motion of small droplets on a fixed boundary. *Journal of Geometric Analysis*, 10(4):575 – 596, 2000.

[4] S. M. Allen and J. W. Cahn. A microscopic theory for antiphase boundary motion and its application to antiphase domain coarsening. *Acta Metallurgica*, 27(6):1085 – 1095, 1979.

[5] P. W. Bates and P. C. Fife. Spectral comparison principles for the cahn-hilliard and phase-field equations, and time scales for coarsening. *Physica D: Nonlinear Phenomena*, 43(2):335 – 348, 1990.

[6] P. Bollada, C. Goodyer, P. Jimack, A. Mullis, and F. Yang. Three dimensional thermal-solute phase field simulation of binary alloy solidification. *Journal of Computational Physics*, 287, 2015.

[7] P. C. Bollada, C. E. Goodyer, P. K. Jimack, and A. M. Mullis. Simulations of three-dimensional dendritic growth using a coupled thermo-solutal phase-field model. *Applied Physics Letters*, 107(5):053108, 2015.

[8] J. Bosch, C. Kahle, and M. Stoll. Preconditioning of a coupled cahn-hilliard navier-stokes system. *Communications in Computational Physics*, 23:603–628, 2018.

[9] D. Broutman. A practical guide to pseudospectral methods. *Journal of Fluid Mechanics*, 360:375?378, 1998.

[10] J. W. Cahn and J. E. Hilliard. Free energy of a nonuniform system. i. interfacial free energy. *The Journal of Chemical Physics*, 28(2):258–267, 1958.

[11] L.-Q. Chen. Phase-field models for microstructure evolution. *Annual Review of Materials Research*, 32(1):113–140, 2002.

[12] K. Cheng, W. Feng, C. Wang, and S. M. Wise. An energy stable fourth order finite difference scheme for the cahnhilliard equation. *Journal of Computational and Applied Mathematics*, 2018.

[13] A. Christlieb, J. Jones, K. Promislow, B. Wetton, and M. Willoughby. High accuracy solutions to energy gradient flows from material science models. *Journal of Computational Physics*, 257:193 – 215, 2014.

[14] J. D. de St. Germain, J. McCorquodale, S. G. Parker, and C. R. Johnson. Uintah: a massively parallel problem solving environment. In *Proceedings the Ninth International Symposium on High-Performance Distributed Computing*, pages 33–41, 2000.

[15] A. E. Diegel, C. Wang, and S. M. Wise. Stability and convergence of a second-order mixed finite element method for the CahnHilliard equation. *IMA Journal of Numerical Analysis*, 36(4):1867–1897, 2015.

[16] Q. Du, L. Ju, X. Li, and Z. Qiao. Stabilized linear semi-implicit schemes for the nonlocal Cahn-Hilliard equation. *JOURNAL OF COMPUTATIONAL PHYSICS*, 363:39–54, JUN 15 2018.

[17] Q. Du and R. A. Nicolaides. Numerical analysis of a continuum model of phase transition. *SIAM Journal on Numerical Analysis*, 28(5):1310–1322, 1991.

[18] D. J. Eyre. Unconditionally gradient stable time marching the cahnhilliard equation. *MRS Proceedings*, 529:39, 1998.

[19] J. Gan and G. Zha. Near field sonic boom calculation of benchmark cases. In *53rd AIAA Aerospace Sciences Meeting*. American Institute of Aeronautics and Astronautics Inc, AIAA, 2015.

[20] N. Gavish, J. Jones, Z. Xu, A. Christlieb, and K. Promislow. Variational models of network formation and ion transport: Applications to perfluorosulfonate ionomer membranes. *Polymers*, 4(1):630–655, 2012.

[21] N. Gavish, J. Jones, Z. Xu, A. Christlieb, and K. Promislow. Variational models of network formation and ion transport: Applications to perfluorosulfonate ionomer membranes. *Polymers*, 4, 12 2012.

[22] U. Ghia, K. N. Ghia, and C. T. Shin. High-re solutions for incompressible flow using the navier-stokes equations and a multigrid method. *Journal of Computational Physics*, 48:387–411, 1982.

[23] J. Guo, C. Wang, S. Wise, and X. Yue. An h2 convergence of a second-order convex-splitting, finite difference scheme for the three-dimensional cahnhilliard equation. *Communications in Mathematical Sciences*, 14:489–515, 2016.

[24] E. Hairer, S. Nørsett, and G. Wanner. *Solving Ordinary Differential Equations II: Stiff and Differential-Algebraic Problems*. Lecture Notes in Economic and Mathematical Systems. Springer, 1993.

[25] Z. Hu, S. Wise, C. Wang, and J. Lowengrub. Stable and efficient finite-difference nonlinear-multigrid schemes for the phase field crystal equation. *J. Comput. Physics*, 228:5323–5339, 2009.

[26] S. Hysing, S. Turek, D. Kuzmin, N. Parolini, E. Burman, S. Ganesan, and L. Tobiska. Quantitative benchmark computations of two-dimensional bubble dynamics. *International Journal for Numerical Methods in Fluids*, 60(11):1259–1288, 2009.

[27] D. Jeong, Y. Choi, and J. Kim. A benchmark problem for the two- and three-dimensional cahn hilliard equations. *Communications in Nonlinear Science and Numerical Simulation*, 61:149 – 159, 2018.

[28] A. Jokisaari, P. Voorhees, J. Guyer, J. Warren, and O. Heinonen. Benchmark problems for numerical implementations of phase field models. *Computational Materials Science*, 126:139 – 151, 2017.

[29] M. Jones, W. Watson, and T. Parrott. *Benchmark Data for Evaluation of Aeroacoustic Propagation Codes with Grazing Flow*, pages 2005–2853. American Institute of Aeronautics and Astronautics, 2019/04/02 2005.

[30] L. Ju, X. Li, Z. Qiao, and H. Zhang. Energy stability and error estimates of exponential time differencing schemes for the epitaxial growth model without slope selection. *Mathematics of Computation*, 87:1859–1885, 2018.

[31] L. Modica and S. Mortola. Un esempio di γ-convergenza. *Boll. Un. Mat. Ital.*, 14(5):285–299, 1977.

[32] R. L. Pego. Front migration in the nonlinear cahn-hilliard equation. *Proceedings of the Royal Society of London A: Mathematical, Physical and Engineering Sciences*, 422(1863):261–278, 1989.

[33] L. Reyna, M. J. W. Y, and D. T. C. Lange. Metastable internal layer dynamics for the viscous cahn-hilliard equation. *Methods and Appl. of Anal*, 2:285–306, 1995.

[34] O. Savin. Phase transitions, minimal surfaces and a conjecture of de giorgi. *Current Developments in Mathematics 2009*, 101(3):59 – 113, 2010.

[35] J. Shen, J. Xu, and J. Yang. The scalar auxiliary variable (sav) approach for gradient flows. *Journal of Computational Physics*, 353:407 – 416, 2018.

[36] P. Sternberg. The effect of a singular perturbation on nonconvex variational problems. *Arch. Rational Mech. Anal.*, 101(3):209 – 260, 1988.

[37] W. Steven, J. Kim, and J. Lowengrub. Solving the regularized, strongly anisotropic cahnhilliard equation by an adaptive nonlinear multigrid method. *Journal of Computational Physics*, 226(1):414 – 446, 2007.

[38] U. Trottenberg, C. Oosterlee, and A. Schüller. *Multigrid*. Academic Press, New York, 2001.

[39] B. P. Vollmayr-Lee and A. D. Rutenberg. Fast and accurate coarsening simulation with an unconditionally stable time step. *Phys. Rev. E*, 68:066703, Dec 2003.

[40] B. Wetton. 1D Cahn Hilliard Computation (YouTube Video). https://www.youtube.com/watch?v=cq2o2AUUXGM, September 2015.

[41] B. Wetton. 2D Allen Cahn Simulation (YouTube Video). https://www.youtube.com/watch?v=6ojleQaCuyE, March 2018.

[42] B. Wetton. 2D Cahn Hilliard Energy Simulation (YouTube Video). https://youtu.be/MovUu2DwWvI, February 2018.

[43] B. Wetton. 2D periodic Cahn Hilliard Simulation (YouTube Video). https://www.youtube.com/watch?v=nKstgHLuQFs, March 2018.

[44] S. Wise. Unconditionally stable finite difference, nonlinear multigrid simulation of the Cahn-Hilliard-Hele-Shaw system of equations. *J. Sci. Comput.*, 44:38–68, 2010.

[45] S. M. Wise, J. Lowengrub, H. B. Frieboes, and V. Cristini. Three-dimensional multispecies nonlinear tumor growth–i model and numerical method. *Journal of theoretical biology*, 253 3:524–43, 2008.

[46] J. Xu, Y. Li, S. Wu, and A. Bousquet. On the Stability and Accuracy of Partially and Fully Implicit Schemes for Phase Field Modeling. *ArXiv e-prints*, Apr. 2016.

[47] Y. Yan, W. Chen, C. Wang, and S. Wise. A second-order energy stable bdf numerical scheme for the cahn-hilliard equation. *Communications in Computational Physics*, 23:572–602, 2018.

[48] F. Yang. Phase Field Benchmarking (Github Repository). https://github.com/timondy/PhaseFieldBenchmarking, December 2018.

[49] F. Yang, C. Goodyer, M. Hubbard, and P. Jimack. An optimally efficient technique for the solution of systems of nonlinear parabolic partical differential equations. *Advances in Engineering Software*, 103, 2017.

[50] P. Yue, J. J. Feng, C. Liu, and J. Shen. A diffuse-interface method for simulating two-phase flows of complex fluids. *Journal of Fluid Mechanics*, 515:293317, 2004.